Metal-enriched atmospheres in warm (super- and sub-) Neptunes induced by extreme atmospheric escape

Louca, A.J.; Miguel, Y.

Citation

Louca, A. J., & Miguel, Y. (2025). Metal-enriched atmospheres in warm (super- and sub-) Neptunes induced by extreme atmospheric escape. *The Astrophysical Journal*, *991*(1). doi:10.3847/1538-4357/add736

THE ASTROPHYSICAL JOURNAL, 991:121 (11pp), 2025 September 20 https://doi.org/10.3847/1538-4357/add736

Metal-enriched Atmospheres in Warm (Super- and Sub-) Neptunes Induced by Extreme Atmospheric Escape

Amy J. Louca[1] and Yamila Miguel[1,2]
[1] SRON Netherlands Institute for Space Research, Niels Bohrweg 4, 2333 CA, Leiden, The Netherlands; louca@strw.leidenuniv.nl
[2] Leiden Observatory, Leiden University, Einsteinweg 55, 2333 CC, Leiden, The Netherlands

Received 2024 June 20; revised 2025 May 8; accepted 2025 May 8; published 2025 September 19

Abstract

Planet formation impacts exoplanet atmospheres by accreting metals in solid form, leading to atmospheric carbon-to-oxygen ratios (C/O) and sulfur-to-nitrogen ratios (S/N) that deviate from those of their host stars. Recent observations indicate differing metal abundances in planetary atmospheres compared to their stellar companions. However, these observations are biased toward mature planets, raising questions about whether these abundances result from formation or evolved over time. Another way to alter an atmosphere is through the escape of particles due to thermal heating. This study examines how billions of years of particle escape affect metal abundances. Using an adjusted stellar evolution code incorporating hydrodynamic escape, we model a warm ($T_{\rm eq} \approx 1000$ K) super-Neptune-type planet ($M_{\rm ini} = 26 M_\oplus$) orbiting a solar-type star. Our results show increased metal-to-hydrogen abundances of ~50–70 × initial enrichment after 10 Gyr. We also see a 0.88 × decrease in C/O abundance and a 1.27 × increase in S/N abundance, which can affect the interpretation of planet formation parameters. We also simulate the evolving atmosphere using chemical kinetics and radiative transfer codes, finding substantial increases in SO_2, CO_2, and H_2O abundances and a decrease in CH_4 abundance. These changes are easily observable in the IR wave band transmission spectrum. Our findings demonstrate that extreme escape of lighter particles significantly influences the evolution of warm Neptunes and complicates the interpretation of their observational data. This highlights the need to consider long-term atmospheric evolution in understanding exoplanet compositions.

Unified Astronomy Thesaurus concepts: Exoplanets (498); Exoplanet atmospheric evolution (2308); Exoplanet evolution (491); Hydrodynamics (1963)

1. Introduction

It is believed that the formation sites of exoplanets leave an imprint on their composition (K. I. Öberg et al. 2011). The temperature gradient within protoplanetary disks creates ice lines at various distances from the host star, leading to the accretion of heavy atoms in solid, molecular form during planet formation. Consequently, in planetary atmospheres, this changes metal (i.e., atoms heavier than H and He) ratios, such as the carbon-to-oxygen ratio (C/O). Observations have shown that the metal abundance of planetary atmospheres is indeed different with respect to the composition of their host star (e.g., L. Alderson et al. 2023; J. L. Bean et al. 2023). However, a substantial part of these planets have evolved for several billion years, raising the question of whether this observed heavy metal abundance is an imprint from formation or has changed over time.

There are several ways to potentially alter a planetary atmosphere over time, one of which is the escape of particles due to thermal heating. Exoplanets with short orbital periods endure extreme escape throughout their lifetime. X-ray and ultraviolet (XUV) heating from their host star results in an upward bulk motion of particles within the atmospheres, known as hydrodynamic escape, and is the main driver of extreme atmospheric evaporation (C. P. Johnstone et al. 2015). With sufficient energy from the stellar XUV irradiation, the velocity of the particles exceeds the escape velocity, $v_{\rm esc}$, and eventually surpasses the Roche-lobe radius. At this point, the particles become unbound to the planet. Light particles, such as hydrogen and helium, suffer most from this escape mechanism. In some cases, the escape of these light gases is so extreme that they can drag along heavy metals (i.e., particles with an atomic mass larger than helium). This was first observed by A. Vidal-Madjar et al. (2004) for the escape of oxygen and carbon on HD 209458 b and subsequently also for other metals such as Si, S, and Fe on various types of hot gaseous planets (see, e.g., J. L. Linsky et al. 2010; E. Schlawin et al. 2010; L. A. Dos Santos 2023). The amount of metals escaping depends on the momentum gained by the drag of the extreme hydrogen upflow. To obtain enough momentum for exceeding $v_{\rm esc}$, the downward gravitational force should be smaller than the upward heating force. This gravitational force is directly proportional to the escaping body mass, $F_g \propto m$ (where F_g is the gravitational force and m is the escaping body mass). Higher particle masses, therefore, need more heat transfer to obtain the same escape velocity as lower particle masses. Assuming that the heat transfer has the same efficiency for all particles, heavier particles are expected to have a less extreme escape. Naturally, a discrepancy emerges between the relative particle abundances, and we expect to see fractionation between metals of different masses.

This has been theoretically worked out by D. M. Hunten et al. (1987), where they defined the crossover mass to include the drag of heavy elements in their mathematical framework of particle escape. In this work, they focused on hydrogen-dominated atmospheres of Mars-/Earth-like size to explain the currently found mass-dependent depletion of the noble gases within the atmospheres of Mars and Earth. Their results showed that a substantial mass fractionation of heavy gases is expected to emerge due to hydrodynamic escape. This could result in changing relative metallic content within exoplanet atmospheres. In contrast, C. Mordasini et al. (2016) showed that formation is the dominating process in defining planetary spectra. They included both formation and evolution models of the planet that take envelope evaporation into account. Their main focus is, however, on relatively massive hot Jupiters (see also A. J. Louca et al. 2023), and it is argued in their study that envelope evaporation is not the dominating process. They, therefore, do not include mass fractionation on these planets and use formation models to explain their planetary spectra.

Working further on these results, we investigate the effect of hydrodynamic escape on the mass fractionation of metals like carbon (C), nitrogen (N), oxygen (O), sulfur (S), magnesium (Mg), silicon (Si), and iron (Fe) within a warm super-Neptune orbiting a solar-like star that could be easily observed using current state-of-the-art observing facilities. Using planetary evolution models that take extreme atmospheric escape into account, we look at the effect of metal drag on the mass fractionation of heavy metals to ultimately find out whether formation creates an imprint on spectral features or whether we should consider the atmospheres to be more dynamic over time than initially thought. This is important in explaining and correctly interpreting currently observed planetary spectra. In the next section, we lay out the methodology and then discuss the results in Sections 3 and 4.

2. Methodology

The methodology in this study has two main steps. First, planetary evolution is simulated to evaluate how extrinsic parameters such as mass, radius, and metallicity evolve (Section 2.1). These parameters are then forwarded to a radiative transfer and chemical kinetics code to see how the atmosphere evolves consequently (Section 2.2).

2.1. Planetary Evolution

2.1.1. Metal Drag

The planetary interior and envelope are evolved by making use of an adapted version of the Modules for Experiments in Stellar Astrophysics, `MESA` (B. Paxton et al. 2011, 2013, 2015, 2018, 2019; A. S. Jermyn et al. 2023). Hydrodynamic escape is included in the form of a hydro-based approximation (HBA; D. Kubyshkina et al. 2018, 2020). We make use of the MIST database (J. Choi et al. 2016; A. Dotter 2016; B. Paxton et al. 2011, 2013, 2015) to update the stellar flux as a function of time within the `MESA` simulations. We obtain time-dependent planet characteristics such as its mass and radius from these simulations.

Using these characteristics, the metallicity of the envelope is evaluated posteriorly (see A. J. Louca et al. 2023). We assume a simple model of metal drag to estimate the mass fractionation of metals. The crossover mass from the model dictates whether metal drag must be factored in. If the mass of the minor species within the atmosphere is lower than the crossover mass, it will be dragged along with the bulk motion of the major escaping species. Contrariwise, if the mass of the secondary species is higher than the crossover mass, it will remain in the atmosphere. The crossover mass is defined as

$$m_c = m_1 + \frac{kTF_1}{bgX_1}, \tag{1}$$

where m_c is the crossover mass, m_1 is the mass of the primary species (i.e., hydrogen), T is the equilibrium temperature, F_1 is the escape flux of the primary species, X_1 is the mixing ratio of the bulk gas in the atmosphere, k is the Boltzmann constant, b is the binary diffusion parameter, and g is the gravitational acceleration of the planet.

The escape flux of the primary species is dependent on the received stellar XUV flux, which relaxes over time (see the detailed formulation in D. Kubyshkina et al. 2018, hereafter K18). This causes the crossover mass to decrease as the system evolves and slowly becomes smaller than the atomic mass of the secondary species. We therefore expect to see less metal drag over time, depending on the atomic mass of the secondary species. Heavier particles, such as sulfur, will fall above the crossover mass threshold sooner than lighter particles, such as nitrogen, oxygen, and carbon. This discrepancy in the degree of metal drag will, therefore, lead to a relative change in abundance between metals.

We simulate a warm super-Neptune, with an initial mass of $M = 26\ M_\oplus$ and an initial envelope mass fraction of $f = 0.55$. We assume a solid rocky core that consists of silicates and heavier metals, similar to Earth's core. The envelope is assumed to be hydrogen-dominated, with solar abundance, and homogeneously mixed. The planet orbits a solar-like host star at 0.075 au, giving it an equilibrium temperature of $T_{\rm eq} \sim 1000$ K.

Finally, metal drag highly depends on equilibrium temperature. This is because the escape flux of the major species is, in the least extreme scenario, proportional to $\dot{M}_1 \propto T_{\rm eq}^{-3.7489}$ (see K18), and the escape flux of the secondary species is directly proportional to the escape flux of the primary species. Hence, changing the temperature alters metal drag by almost 4 orders of magnitude.

Furthermore, a decrease in temperature also lowers the crossover mass, which results in lower escape ages. To investigate the influence of temperature on the metal enhancement within atmospheres, we vary the semimajor axis between 0.075 and 0.15 au, giving a temperature range of $T_{\rm eq} \approx$ 700–1000 K and a binary diffusion parameter range of $b/10^{19} \approx 3.22$–$3.98\ {\rm cm^{-1}\ s^{-1}}$ (following T. R. Marrero & E. A. Mason 2009).

2.1.2. Fractionation: Time-dependent Escape Flux

Metal fractionation is calculated by considering an upward metal flux that changes over time and depends on the major escaping species in the atmosphere. In particular, this upward metal flux depends on the upward flux of the major escaping species and their abundance (see chapter 5 of D. Catling & J. Kasting 2017),

$$F_2 = \frac{n_2}{n_1} F_1 \left(\frac{m_c - m_2}{m_c - m_1} \right), \tag{2}$$

where subscripts 1 and 2 denote the major and minor species, respectively. In this case, the major species that suffers from hydrodynamic escape is hydrogen, and the minor species that get dragged along with it are the metals carbon, nitrogen, oxygen, and sulfur. Here, F is the escape flux, n is the number density, and m is the species mass. Note that the volume factor of the number densities cancels out in Equation (2), and we can, thus, also consider N to be the full content of particles within the envelope of planets. Similarly, the flux terms both depend on the same surface area of the planet, and we can consider those as the mass loss in grams per second,

$$\dot{M}_2 = \frac{N_2}{N_1}\dot{M}_1\left(\frac{m_c - m_2}{m_c - m_1}\right). \quad (3)$$

The mass loss of the main escaping species due to hydrodynamic escape processes, $\dot{M}_1$, is calculated using the hydrodynamic escape approximation from K18,

$$\dot{M}_1 = e^{\beta}(F_{\mathrm{XUV}})^{\alpha_1}\left(\frac{a}{\mathrm{au}}\right)^{\alpha_2}\left(\frac{R_{\mathrm{pl}}}{R_{\oplus}}\right)^{\alpha_3}\Lambda^{K}, \quad (4)$$

where the parameters β, α_1, α_2, and α_3 can be found in Table 1 of K18, F_{XUV} is the XUV irradiation flux from the host star, a is the orbital distance, R_{pl} is the planetary radius, Λ is the Jeans escape parameter, and K describes how fast the mass-loss rates decrease with increasing Λ, as defined in K18. This expression is an analytical approximation of the actual hydrogen mass loss based on a grid of hydrodynamical simulations. The fractionation between metals can be calculated using this upward escape flux of metals due to drag. In particular, the number of metal particles is updated using

$$N_{z_t} = N_{z_{t-1}} - \frac{1}{m_z}\int_{t-1}^{t}\dot{M}_2(t)\mathrm{d}t, \quad (5)$$

where m_z is the mass of the metal. The metal mass fraction is then updated by summing over all updated total metal masses,

$$Z_t = \frac{\sum_z N_{z_t}\cdot m_z}{M_{\mathrm{env}}}, \quad (6)$$

where M_{env} is the envelope mass of the planet. The mass fraction of hydrogen is then updated by assuming that the hydrogen-to-helium mass fraction (X/Y) remains the same, which is a valid assumption for Neptune-sized planets that have a large envelope fraction (I. Malsky & L. Rogers 2020). Since the hydrogen-to-helium fraction remains the same and all mass fractions must add up to 1 ($X + Y + Z = 1$), we update the hydrogen mass fraction using

$$X_t = \frac{1 - Z_t}{1 + 1/C}, \quad (7)$$

where C is the initial hydrogen-to-helium fraction. For these calculations to hold, we use the condition that hydrogen always needs to be the most abundant species in the atmosphere, i.e.,

$$X_t > Z_t. \quad (8)$$

If this condition is no longer satisfied, we will regard the atmospheric escape as too extreme, and the planet will not be considered within the grid simulation.

Finally, the hydrogen content is updated by

$$N_{\mathrm{H}_t} = \frac{X_t\cdot M_{\mathrm{env}}}{m_{\mathrm{H}}}. \quad (9)$$

For initial conditions, we assume solar-like abundance with $X_{t=0} = 0.74$ and number density ratios from M. Asplund et al. (2009). We only consider the most abundant volatile and metal species, C, N, O, Mg, Si, S, and Fe.

2.2. *Atmospheric Evolution*

We continue this modeling setup for a planet with initial parameters of $M = 26\ M_{\oplus}$ and $f_{\mathrm{env}} = 0.55$ that orbits a solar-type star at 0.075 au. All planet characteristics, such as mass, radius, and metallicity, are updated according to the results from the planetary evolution code.

2.2.1. *Temperature–Pressure Profiles*

The thermal structures in the planet's atmosphere are updated using the open-source radiative transfer code `HELIOS` (M. Malik et al. 2017, 2019). The thermal profile of the planet is evaluated in six steps, during which the planet's radius, mass, and metallicity are updated according to all previous results. We keep stellar parameters constant to evaluate only the impact of hydrodynamic escape on the atmosphere. All included opacity sources are listed in Table 1. We consider pressure broadening due to H_2 collisions for the atoms Na and K up until 100 bar. The k-tables are sampled for a wavelength range of 0.06–200 μm, with a resolution element of $\lambda/\Delta\lambda = 1000$, and assuming chemical equilibrium for all species abundances using the open-source chemical equilibrium code `FastChem` (J. Stock et al. 2018). Furthermore, we assume an internal temperature of $T_{\mathrm{int}} = 200$ K, a global heat redistribution factor of 0.33, and isotropic irradiation from the host star.

2.2.2. *Chemical Evolution*

After having obtained the temperature profiles of the planet, the composition of the atmosphere is calculated using the (photo-)chemical kinetics code VULCAN (S.-M. Tsai et al. 2017, 2021). The chemical composition of the atmosphere is also determined for six time steps. The planet's radius, mass, metallicity, and thermal profile are updated at each time step. Metals included in the chemical network are C, N, O, and S. The chemical network comprises 574 forward and backward reactions and 68 photochemical reactions. For the photochemical reactions, we include the stellar spectrum of the Sun from C. A. Gueymard (2003). Like before, all abundances are initialized with the open-source chemical equilibrium code `FastChem`. Vertical mixing is considered in the form of both molecular and eddy diffusion. For the eddy diffusion constant, we use a constant profile of $K_{zz} = 10^{10}$, which has been previously used by other studies (e.g., J. I. Moses et al. 2013; V. Parmentier et al. 2013; Y. Miguel & L. Kaltenegger 2014).

2.2.3. *Transmission Spectra*

For the final modeling step, the different atmospheres are forwarded to the radiative transfer code petitRADTRANS (P. Mollière et al. 2019, 2020; E. Alei et al. 2022) to obtain the transmission spectra at each of the six time steps. All spectra are created assuming the opacity of the species H_2O, CH_4, SO_2, CO_2, CO, NH_3, H_2S, and H_2 (as listed in Table 1), and include collisional induced absorption of H_2–H_2 and H_2–He. The resolution element for all opacity sources is $\lambda/\Delta\lambda = 1000$.

3. Results

This section presents the findings related to planetary evolution and its impact on metal enhancement (Section 3.1). Following this, we focus on atmospheric evolution and its observational implications (Section 3.2).

Table 1
The Line Lists Used for Each Opacity Species Included in Radiative Transfer

Molecule	Temperature Range (K)	Pressure Range (bar)	Line Lists `HELIOS`	Line Lists `pRT`
H_2O	50–2900	10^{-8}–10^3	POKAZATEL (1)	POKAZATEL (1)
CH_4	50–2900	10^{-8}–10^3	YT34to10 (2)	YT34to10 (2)
SO_2	50–2900	10^{-8}–10^3	ExoAmes (v2) (3)	ExoAmes (v2) (3)
CO	50–2900	10^{-8}–10^3	Li2015 (4)	HITEMP (11)
H_2S	50–2900	10^{-8}–10^3	AYT2 (5)	AYT2 (5)
CO_2	50–2900	10^{-8}–10^3	CDSD-4000 (6)	UCL-4000 (12)
PH_3	50–2900	10^{-8}–10^3	SAITY (7)	N/A
NH_3	50–2900	10^{-8}–10^3	N/A	CoYuTe (13)
H_2	50–2900	10^{-8}–10^3	RACPPK (8)	N/A
Atom				
H	2500–6100	10^{-8}	VALD (9)	N/A
He	2500–6100	10^{-8}	Kurucz (10)	N/A
Na	2500–6100	10^{-8}	Allard19 (14)	N/A
K	2500–6100	10^{-8}	Allard16 (15)	N/A

References. (1) O. L. Polyansky et al. (2018); (2) S. N. Yurchenko & J. Tennyson (2014); S. N. Yurchenko et al. (2017); (3) D. S. Underwood et al. (2016); (4) G. Li et al. (2015); W. Somogyi et al. (2021); (5) A. A. A. Azzam et al. (2016); K. L. Chubb et al. (2018); (6) S. Tashkun & V. Perevalov (2011); (7) C. Sousa-Silva et al. (2014); (8) E. Roueff et al. (2019); (9) N. E. Piskunov et al. (1995); (10) R. L. Kurucz & B. Bell (1995); (11) L. Rothman et al. (2010); (12) S. N. Yurchenko et al. (2020); (13) P. A. Coles et al. (2019); (14) N. F. Allard et al. (2019); (15) N. F. Allard et al. (2016).

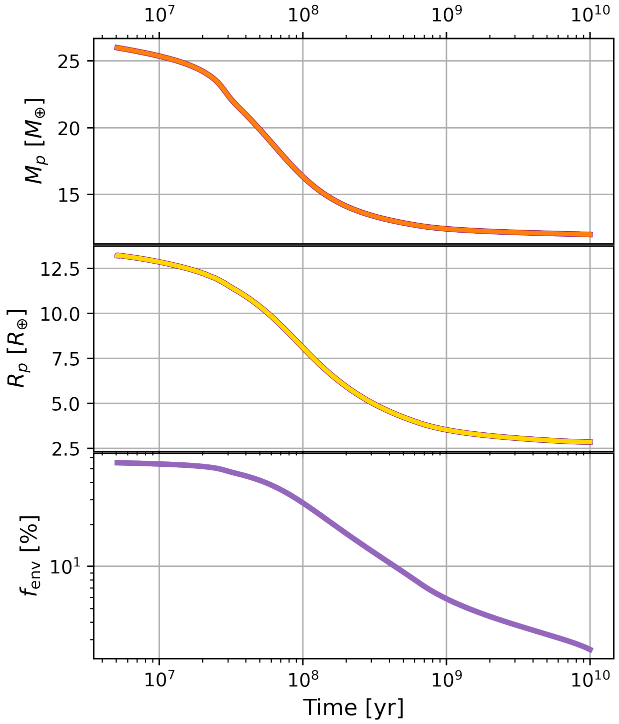

Figure 1. The evolution of the mass (upper panel), radius (middle panel), and envelope mass fraction (lower panel) of a planet with an initial mass of $M = 26\ M_\oplus$ and initial envelope mass fraction of $f_{\rm env} = 55\%$ orbiting a solar-like host star at a distance of $a = 0.075$ au.

3.1. Planetary Evolution

3.1.1. Mass, Radius, and Envelope

The planet in this study is born a super-Neptune. Due to its relatively high equilibrium temperature (∼1000 K) and high initial envelope mass fraction, the planet suffers from great mass losses of its hydrogen-dominated envelope, as seen in Figure 1. After ∼1–2 Gyr, the super-Neptune has evolved into a sub-Neptune-type planet. Most of its mass is lost in the first ∼20–100 Myr of the evolution, which is also the period it contracts most. During this period, the extreme escape of hydrogen is expected to drag along most metals. After 10 Gyr, the final density has converged to ~ 2.85 g cm^{-3}, with an envelope mass fraction of ∼2.5%, leaving the planet with a planed, but still observable, gaseous envelope.

3.1.2. Metal Mass Loss

The mass loss of each metallic species due to drag depends on three factors, one of which is the same for each metal (i.e., the escape flux of the minor species, see Equation (2)). However, each metal's atomic mass and relative abundance differ, which causes a difference in final mass loss per atom. The middle panel of Figure 2 illustrates this difference in mass loss for each of the species. The relative difference between the total envelope mass loss and the metal mass loss (gray line) decreases over time, from ∼3 orders of magnitude to ∼2 orders of magnitude.

Both the sulfur and iron mass loss show an asymptotic behavior around ∼7–8 Gyr and ∼4–5 Gyr, respectively, wherein they drop to zero. This is because, around these periods, the crossover mass falls below the atomic mass of sulfur and iron, as seen in the top panel of Figure 2. At the same time, it can be seen in the bottom panel that the minimum stellar flux needed to drag these elements is higher than the incident stellar flux at that time. This indicates that hydrogen does not get enough stellar energy to drag along elements such as iron and sulfur. Similarly, the mass loss of silicon also shows a steep drop around ∼ 9 Gyr but continues to escape shortly after. This is due to the slightly increasing crossover mass at ∼ 9 Gyr. Lighter metals such as oxygen, nitrogen, and carbon do not show this asymptotic trend since they always fall below the crossover mass during the evolution and will, therefore, always be dragged along and escape. This contrasting behavior between metals is thought to cause a relative enhancement in heavier metals, such as sulfur and iron.

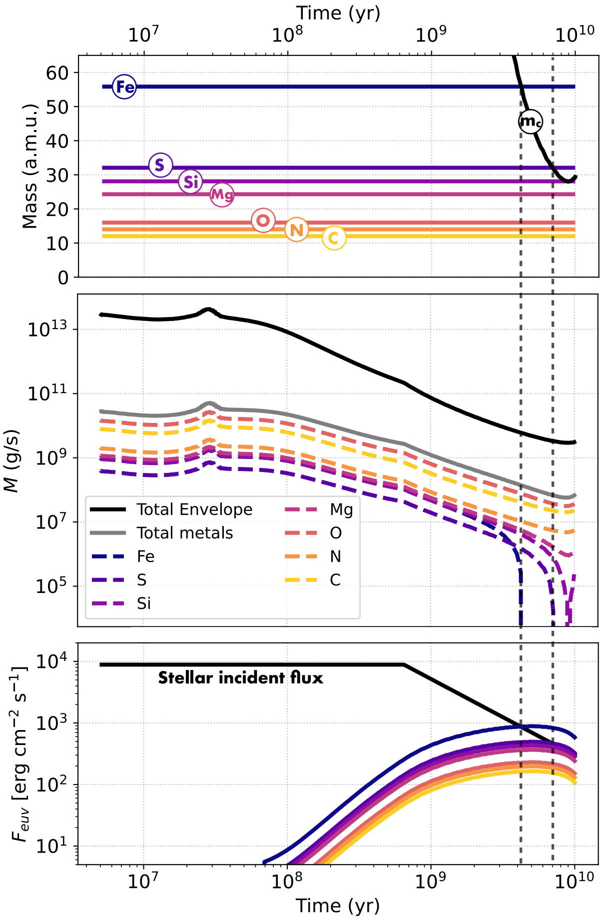

Figure 2. The evolution of the crossover mass (black solid line, top panel), the evolution of the total mass loss of each element (middle panel), and the evolution of the incoming $F_{\rm euv}$ irradiation of the host star (bottom panel) for a planet with mass $M = 26M_\oplus$, an initial envelope fraction $f_{\rm env} = 0.55$, and a semimajor axis of $a = 0.075$ au. The horizontal colored lines represent the different metallic species considered in this study (i.e., iron, sulfur, silicon, magnesium, oxygen, nitrogen, and carbon) as indicated by colors. The vertical dashed lines indicate the escape age of Fe and S (see text for more details). In the bottom panel, the colored lines represent the minimum stellar flux needed for these species to be dragged with the escaping hydrogen.

The gray line shows the total metal mass loss in Figure 2. Notably, oxygen contributes significantly to the overall metal loss, surpassing the mass loss of nitrogen and carbon, despite its higher atomic mass. This is because the initial abundance of oxygen is relatively high compared to all other metals considered, which shows that initial abundance is a key factor in determining the mass-loss evolution of metals.

3.1.3. The Metal-to-hydrogen Enhancement over Time

Considering all previous results, we anticipate observing a substantial increase in the metal-to-hydrogen ratios. Illustrated in the top panel of Figure 3 is the temporal relative metal enhancement. In this case, metal enhancement means the evolving metal-to-hydrogen ratio normalized by its initial value. This figure shows that most of the metal enhancement should occur after 0.1 Gyr into the simulation, hinting that the first 100 million yr are a window into observing the imprints of planet formation. Shortly after, the metal enhancement increases drastically for all species considered in this study. With a final enhancement of ∼48 × the initial abundance, the least affected species is carbon. The most affected species, iron, shows an increase factor of ∼70 × its initial abundance. This indicates that there is a correlation between atomic metal mass and metal enhancement. The heavier metals (e.g., Si, S, and Fe) have a higher final enhancement over time than the lighter metals (e.g., C, N, and O).

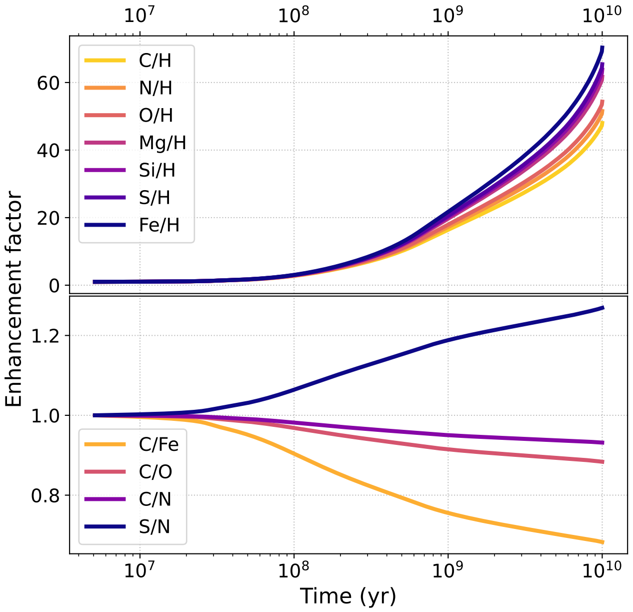

Figure 3. The temporal evolution of the metal-to-hydrogen enhancement (top panel) and of the metal-to-metal enhancement (bottom panel). Note that not all metal-to-metal ratios are shown here, but only the most relevant cases are depicted.

3.1.4. The Metal-to-metal Enhancement over Time

Due to each metal's different mass-loss rate and escape age, the metal-to-metal ratio is also expected to change over time. The bottom panel of Figure 3 illustrates the temporal metal-to-metal ratio for the most extreme and relevant metal ratios. Contrarily to before, it can be seen that the metal fractions have already started to change in the first 100 Myr of evolution. This is due to each species' different mass loss and initial abundance (see Section 3.1.2). After this period, the metal-to-metal enhancement seems to converge for each species. The maximum enhancement can be found in the C/Fe ratio, with a 0.68 × decrease after 10 Gyr.

The C/O is widely used to indicate where the planet formed and is often thought to be static in time. These results show, however, that we expect to see a decrease of 0.88 × after 10 Gyr. Depending on the initial C/O, this decrease in ratio can have implications for inferring the formation sites of planets (K. I. Öberg et al. 2011). A value of $C/O \geqslant 1$ implies that the planet has formed around $a \geqslant 10$ au. A decrease factor of 0.88 × due to evolution can thus temper the inference of formation parameters and should be accounted for. Also considering the possibility of nonconventional C/O values resulting from in situ formation near the soot line (E. A. Bergin et al. 2023), the challenge of linking C/O to planetary formation and evolution is further complicated by the impact of extreme atmospheric escape.

Another indicator for formation sites of exoplanets is the sulfur-to-nitrogen ratio (S/N). In particular, it has been stated that exoplanets are thought to have formed far away from the

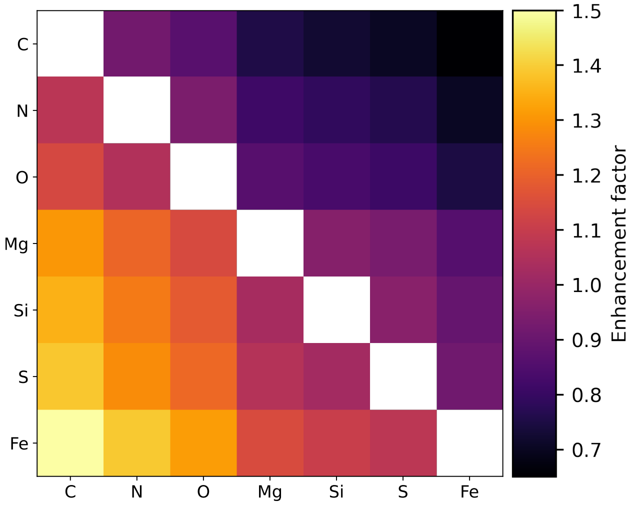

Figure 4. The metal-to-metal enhancement due to metal drag for all the metals considered in this study after 10 Gyr into the simulation. The horizontal and vertical axes denote the metals included and are sorted by their atomic mass.

host star when S/N > C/N (e.g., D. Turrini et al. 2021; E. Pacetti et al. 2022). In this study, we see, however, that planetary evolution can result in an elevated S/N abundance (~1.27 × initial abundance) and a depletion in the C/N abundance (~0.93 × initial abundance), perhaps leading to a false belief that the planet has endured long-term migration.

The final enhancements of all metal combinations are illustrated in Figure 4. This figure shows a color gradient as a function of atomic metal mass: the higher the atomic metal mass ratio discrepancy, the higher the enhancement factor becomes. However, this assumes that the planet's envelope and atmosphere are well mixed and no heavy metal particles sink to the inner parts of the planet due to their relatively high atomic mass.

3.1.5. The Impact of Orbital Distance

The effect of the temperature—and, therefore, semimajor axis—on metal enhancement is shown in Figure 5 (top panel). This figure shows the sulfur-to-hydrogen enhancement as an example case. The enhancement factor decreases substantially when increasing the semimajor axis. This is due to the decreasing irradiation flux from the host star and, therefore, the decreasing equilibrium temperature, limiting the hydrodynamic escape of hydrogen. Even though this would also suggest less metal drag, the metal enhancement is still limited by the restricted amount of hydrogen escape. Similarly, lower equilibrium temperatures also suppress the metal-to-metal ratios in change. The lower panel of Figure 5 shows the evolution of the C/O for four different semimajor axes. For higher semimajor axes and, thus, lower equilibrium temperatures, the change in the C/O abundance becomes less extreme.

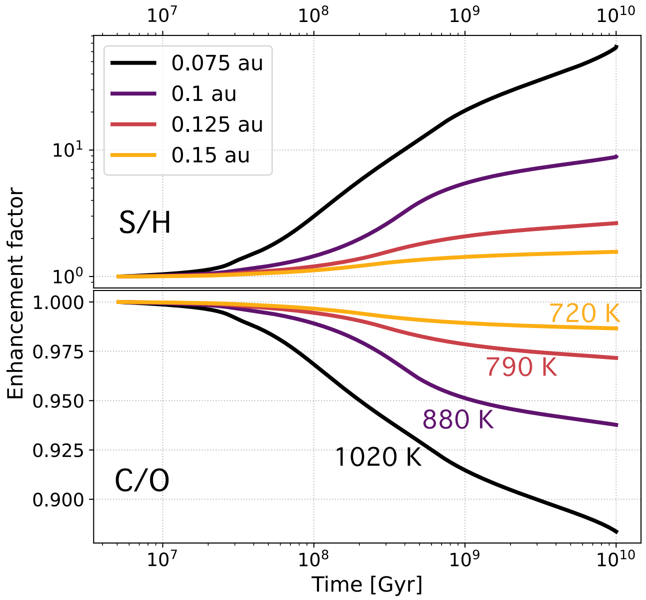

Figure 5. The evolution of the enhancement factors of the sulfur-to-hydrogen ratio (upper panel) and carbon-to-oxygen ratio (lower panel) for four different orbital separations, ranging between 0.075 and 0.15 au.

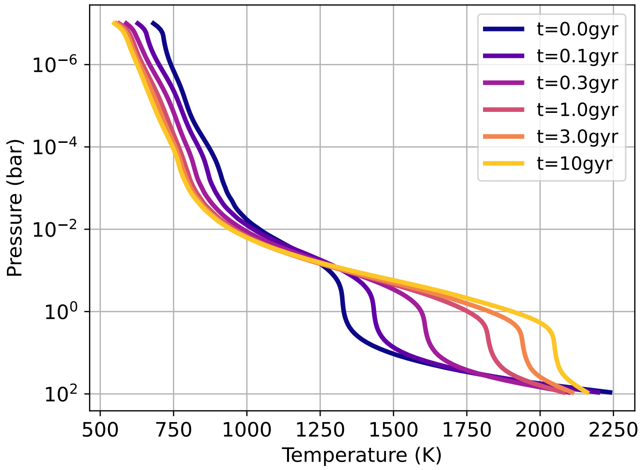

Figure 6. Evolution of the *TP* profile for several time steps, as indicated by colors.

3.2. Atmospheric Evolution

3.2.1. Thermal Evolution

The full thermal evolution of the atmosphere is shown in Figure 6. The biggest atmospheric changes are found in the upper ($P < 10^{-2}$ bar) and lower ($P > 10^{-2}$ bar) regions. Particularly, the upper region shows a decrease in temperature over time, whereas the lower region shows a substantial increase in temperature over time. The upper region shows a change of ~250 K in 10 billion yr, whereas the lower region shows a change of ~750 K.

The increasing metallicity due to extreme atmospheric escape can explain the rising temperature in the lower atmosphere. This causes the atmosphere to contain more H_2O and CO_2, which are greenhouse gases that heat up the atmosphere over time. In particular, this greenhouse effect makes the atmosphere more opaque in the deeper regions around $P \approx$ 0.1–1 bar.

To conserve the global energy within the system, the upper atmosphere cools in response to this increasing temperature in the deeper regions.

3.2.2. Chemical Evolution

The previously presented changes in metallicity, metal-to-metal ratios, and temperature can lead to compositional

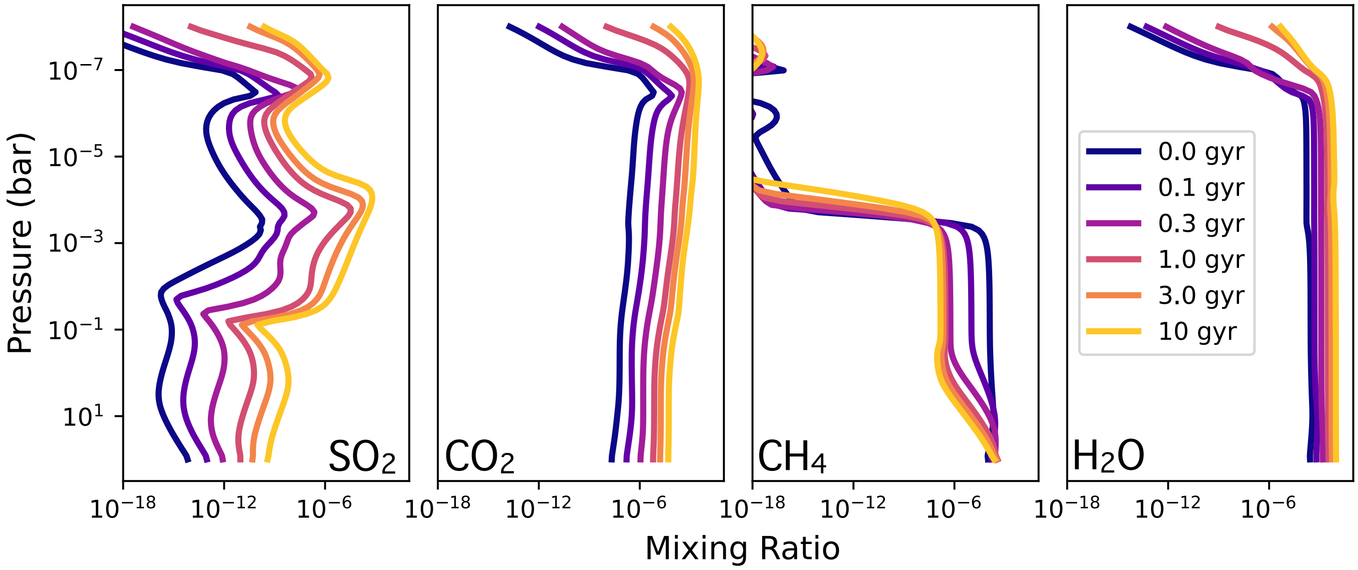

Figure 7. The evolution of the mixing ratio of SO_2, CO_2, CH_4, and H_2O for a planet with an initial mass of $M = 26\ M_\oplus$ and an initial envelope fraction of $f_{\rm env} = 0.55$. The colors in each subplot illustrate the time steps.

changes within planetary atmospheres over time. The full chemical evolution of the species SO_2, CO_2, CH_4, and H_2O is illustrated in Figure 7. Most changes occur between 0.1 and 1.0 Gyr in the evolution of all species. This is when the metallicity changes from $\sim 3 \times$ solar to $\sim 22 \times$ solar. The biggest change can be found in the SO_2 abundance. This relative species abundance increases $\sim$ 7 orders of magnitude over 10 billion yr in nearly all regions of the atmosphere. Both the increase in total metallicity and the increase in the sulfur-to-metal enhancement contribute to this drastic enrichment of SO_2 in the atmosphere. This change in abundance is greatest in the upper atmosphere, with an increase of 11 orders of magnitude. Using a photochemical kinetics model, J. Polman et al. (2023) showed that high-metallicity atmospheres are expected to contain a significant amount of SO_2 abundance, and this was, shortly after, also shown observationally by S.-M. Tsai et al. (2023). Another indicator of high-metallicity atmospheres is the high CO_2 abundance (e.g., K. Lodders & B. Fegley 2002; K. Zahnle et al. 2009; J. I. Moses et al. 2013). From Figure 7, we can see an increase of 3 orders of magnitude in the relative CO_2 abundance throughout the atmosphere due to the increasing metallicity. In the upper atmosphere, this abundance increase goes up to 9 orders of magnitude. The relative H_2O abundance shows the least change throughout the atmosphere, with an increase of ~1–2 orders of magnitude, which can still be regarded as a significant increase in relative abundance. The biggest changes in H_2O can be found in the upper atmosphere, where we see an increase of almost 9 orders of magnitude. Finally, in contrast to the other species, CH_4 shows a depletion of ~4 orders of magnitude in the lower atmosphere. For the deeper regions ($P > 10^{-1}$ bar), this is caused by the drastic increase in temperature in the lower atmosphere, as seen in Figure 6, in combination with vertical mixing and the fact that an increase in metallicity implies less hydrogen available to form methane.

3.2.3. Spectral Evolution

The evolution of the transmission spectrum is illustrated in Figure 8. The biggest changes in spectra can be seen between 0.1 and 1.0 Gyr. During this period, methane-dominated features are transitioned to a mixture of metallic features such as SO_2, CO, and H_2S. Additionally, the water features become more prominent due to increased water abundance over time. More explicitly, we see over time that

1. *0.0–0.1 Gyr (M/H ~ solar).* CH_4 is the dominating species and most prominent in the spectrum. There are other hints of H_2O in the lower wavelength region ($<3\ \mu$m), CO_2 at ~4.4 μm, and NH_3 in the long-wavelength region ($>10\ \mu$m).
2. *0.1–0.3 Gyr (M/H ~ 3–8× solar).* The low-metallicity features of CH_4 (2–8 μm) and NH_3 ($> 10\ \mu$m) start to disappear. Slowly, some higher metallic species such as H_2S (at ~3.8 μm) become more apparent.
3. *0.3–1.0 Gyr (M/H ~ 8–22× solar).* All low-metallicity features, including NH_3, have disappeared from the spectrum. In the long-wavelength region, the SO_2 features at ~7–8 μm start to appear. Additionally, a small CO feature appears around ~ 5 μm.
4. *1–3 Gyr (M/H ~ 22–38× solar).* The SO_2 features become significant within the spectrum at ~4 and 7–8μm.
5. *3–10 Gyr (M/H ~ 38–70× solar).* There is little spectral change besides the bigger high-metallicity features.

Overall, the most significant changes are found in the decreasing CH_4 features at 3–4 μm, which disappear after ~0.1 Gyr after formation, and the increasing SO_2 features at 4 and 7–9 μm.

4. Discussion

This research showed that the influence of extreme atmospheric escape can lead to metal enhancement and fractionation of species for a specific case of a warm super-Neptune. More specifically, the metal-to-hydrogen ratios increased by a factor up to ~50–70 ×, depending on metallic species and planetary system. These results are, however, limited to a few assumptions.

First, the planets were assumed to have a rocky inner core and a homogeneously mixed envelope, though it has been shown in other studies that a compositional gradient might fit

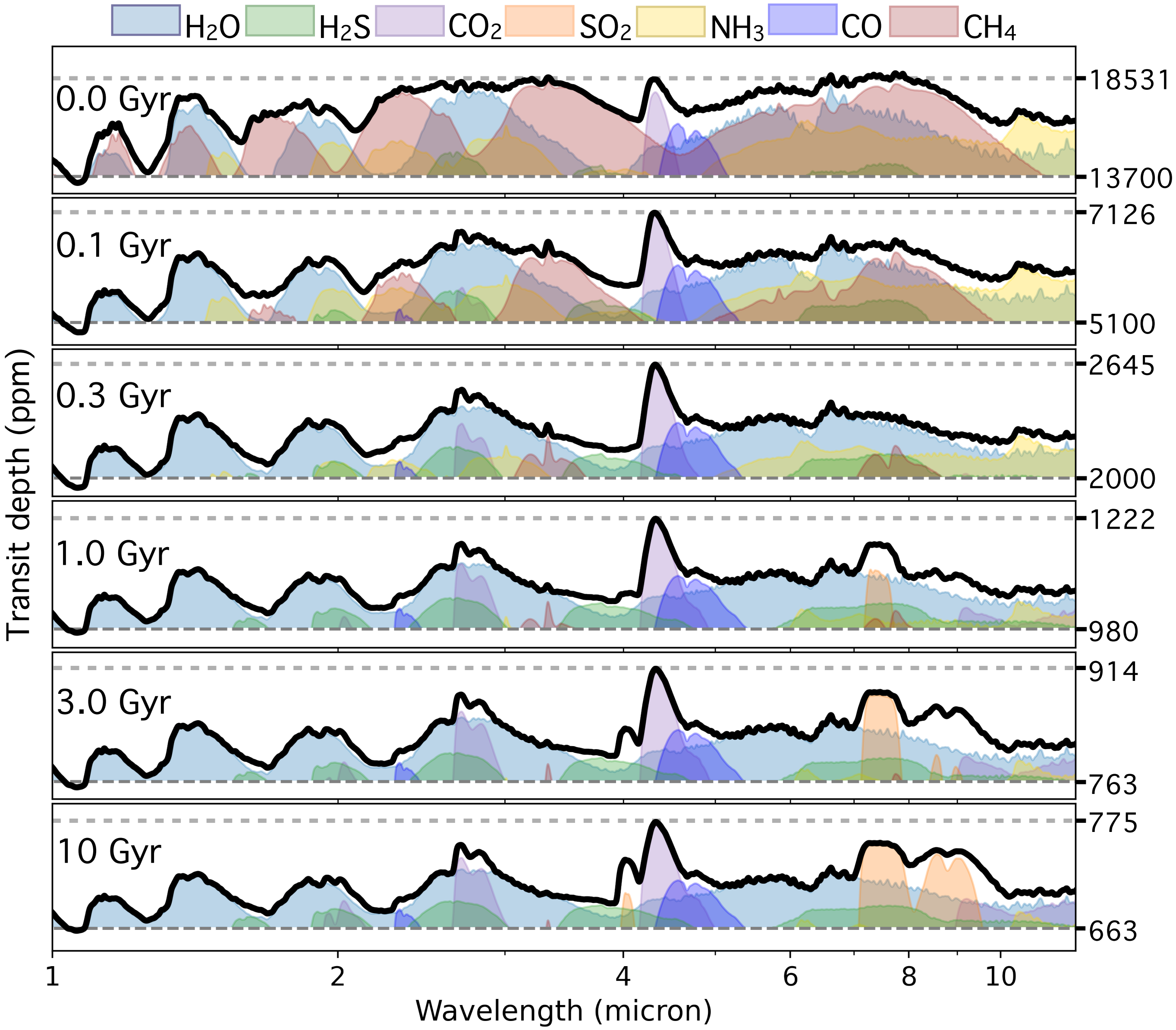

Figure 8. The evolution of the transmission spectrum evaluated at 0, 0.1, 0.3, 1, 3, and 10 Gyr, including the contribution of each species as indicated by color.

better for the planets in our own solar system (e.g., S. M. Wahl et al. 2017; C. R. Mankovich & J. Fuller 2021; Y. Miguel et al. 2022). With such planetary structures, extreme escape from the outer metal-poor atmosphere could expose the inner metal-rich atmosphere, where metal drag becomes less significant. Additionally, metal-enriched envelopes are expected to enhance planetary contraction due to the increased mean molecular weight. In this study, however, metal enrichment was calculated in a posterior manner and, therefore, did not give any feedback to the planetary evolution.

We did not account for stellar evolution or changes in the planet's internal temperature in our atmospheric calculations, though these factors likely alter the *TP* profile, chemistry, and transmission spectra. Additionally, evolving internal temperatures influence the dominant escape mechanism. D. Modirrousta-Galian & J. Korenaga (2023) classify extreme atmospheric escape into time-dependent regimes, with core-powered mass loss driven by residual internal heat. This process can lead to significant atmospheric loss, particularly for planets with thin atmospheres or close to their host star. A. Gupta & H. E. Schlichting (2019) showed that the radius valley can be explained by core-powered mass models. While our study focused on photoevaporation, atmospheric evolution may differ when core-powered mass loss is considered.

Finally, we limited this study to one extreme scenario: a born super-Neptune that evolves into a sub-Neptune over time due to hydrodynamic escape. To see whether the results of extreme metal enhancement due to planetary evolution are limited to only this planet, we performed a grid study where we varied the initial masses (12–26 $M_\oplus$) and envelope mass fractions (0.15–0.55). Figure 9 illustrates the sulfur-to-hydrogen enhancement for the full grid of planets. Each subpanel here also indicates the super-Neptune as presented in Sections 3.1–3.2 with the blue square. Here, we can see that only a select number of planets experience metal enhancement due to hydrodynamic escape, depending on the equilibrium temperature. The super-Neptune of $M = 26\,M_\oplus$ and $f = 0.55$ shifts outside of this region for lower equilibrium temperatures. Overall, we see that for

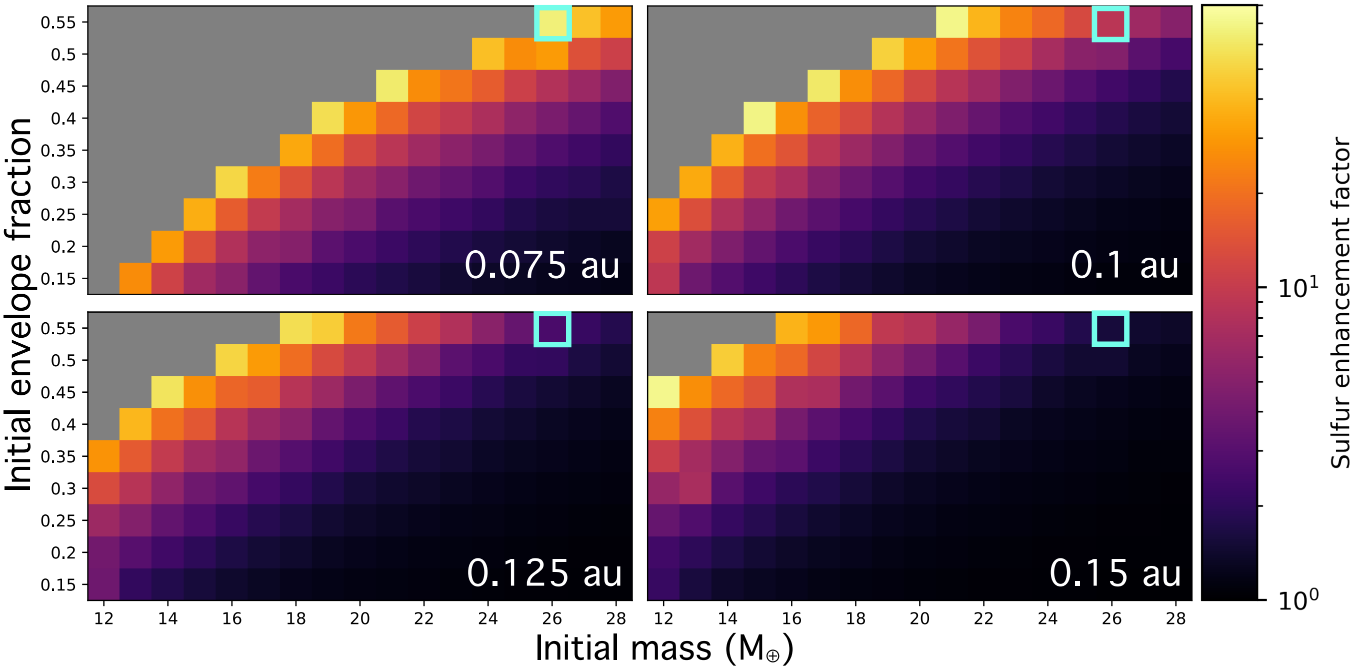

Figure 9. The sulfur enhancement (i.e., $\frac{(S/H)_t}{(S/H)_0}$) evaluated after 10 Gyr for various initial masses, envelope fractions, and orbital distances within the grid space. Each subplot represents the sulfur enhancement for a different orbital distance (0.075–0.15 au), as labeled within the figure. The gray spaces are simulations for which the hydrogen depletion is too strong, and Equation (8) no longer holds. The blue square in each subpanel indicates the previously studied planet with an initial mass of $M = 26\ M_\oplus$ and an initial envelope fraction of $f = 0.55$.

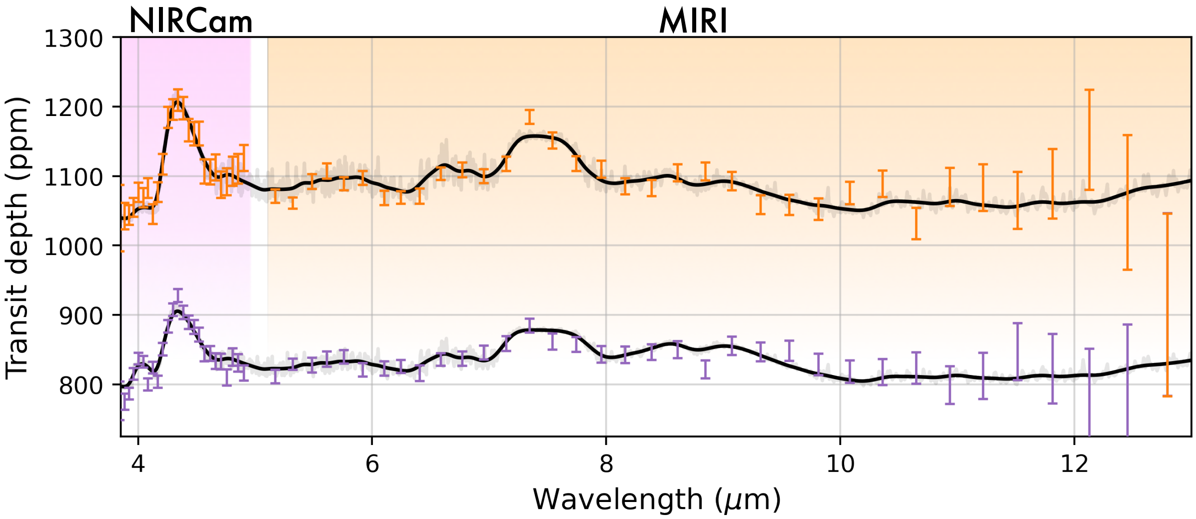

Figure 10. Synthetic (black lines) and synthetic JWST data (orange and purple) for NIRCam F444W and MIRI LRS. The upper transmission spectrum represents the young planet at $t =$ 1 Gyr (orange data points), and the lower transmission spectrum represents the matured planet at $t =$ 3 Gyr (purple data points).

larger semimajor axes, the relative sulfur enhancement becomes less substantial for planets with intermediate-to-high masses and low-to-intermediate envelope fractions. This is due to the lower temperatures causing less extreme hydrogen escape and, therefore, less metal drag overall.

This study also showed that the drastic increase in relative metal abundance can be directly seen in observational transmission spectra in the IR wave band. Such an effect of extreme atmospheric escape on atmospheric composition can be tested observationally by comparing the IR transmission spectrum of adolescent planets with comparable mature planets. Finding suitable targets might still be challenging due to the lack of extremely young planets. This study showed, however, that these planet targets do not necessarily have to be extremely young. A substantial change can still be found in the transmission spectrum between 1 and 3 Gyr. To assess whether these changes in spectra are observable with current state-of-the-art space missions, we create synthetic JWST data using `pandexo` (N. E. Batalha et al. 2017). The most promising features to detect for metallicity enhancement are SO_2, CO_2, and CO between 4 and 10 μm (see Figure 8). The instruments covering these features are the NIRCam F444W mode (4–5 μm) instrument and the MIRI Slitless low resolution spectroscopy (LRS) mode (4.9–27.9 μm) instrument. The predicted transmission spectra for these two instruments are created for a 1 and 3 Gyr planet (from Figure 8), as shown in Figure 10. For both spectra, the data points were created using eight transits for a planet with a transit duration of 0.13375 days orbiting a solar-type star (*J*-magnitude of 7.7). The CO_2 and SO_2 features at ∼4.3 and ∼7.8 μm, respectively, are clearly visible for both spectra. However, the more pronounced SO_2 feature at ∼ 4 μm can only be detected for the more matured planet, as seen in the purple data points of Figure 10. This feature can be used to track the evolution of exoplanets.

5. Conclusion

In this study, we used an extended version of a planetary evolution code that includes the hydro-based approximation to evolve a warm ($T_{\rm eq} \approx 1000$ K) super-Neptune orbiting solar-like star for ∼ 10 Gyr. We used posterior calculations that include metal drag to estimate the metal enhancement for C, N, O, Mg, Si, S, and Fe. To summarize, the results showed that:

1. Heavier species experience less metal drag and, therefore, more metal enhancement.
2. Oxygen contributes most to the total metal mass loss due to its high initial abundance in a solar-like environment.
3. The lighter species carbon, nitrogen, and oxygen are dragged along by the hydrodynamic escape of hydrogen throughout the full evolution for higher-density planets.
4. A maximum metal enhancement of ∼48–70 × the initial metallicity is expected, depending on metal mass.
5. A maximum metal-to-metal enhancement factor of 1.5 × initial enrichment can be found in the carbon-to-iron ratio.
6. The C/O is decreased by a factor of 0.88 × due to planetary evolution and the S/N is increased by a factor of 1.27 ×, both of which impact the interpretation of planet formation parameters.

We also simulated the atmosphere at several time steps using (photo-)chemical kinetics and radiative transfer codes to evaluate chemical composition and spectra evolution. Here, we found that:

1. The upper atmosphere ($P < 10^{-2}$ bar) cools over time, whereas the lower atmosphere ($P > 10$ bar) heats up due to the increasing greenhouse gases (i.e., H_2O and CO_2) in the atmosphere.
2. The SO_2, CO_2, and H_2O abundances show an increase in the upper atmosphere over time due to the increasing metallicity. For SO_2, this increase can even be seen throughout the full atmosphere.
3. Most (spectral) changes can be seen after 0.1 Gyr into the evolution. For $t < 1$ Gyr, the atmosphere consists mainly of methane signatures due to the low metallicity. After this period, a wide variety of high-metallicity features can be seen, such as SO_2, CO, and H_2S.

Overall, this study showed that the evolution of the metal ratios of (volatile) metals are significant for warm (super-) Neptunes with a substantial initial envelope fraction and should be considered when evolving the planet and inferring planet parameters. In several cases, the formation is expected to imprint the metal-to-metal ratios that remain the same throughout the remainder of the planet's lifetime. Nonetheless, this study showed that exoplanets born as (sub- and super-) Neptunes can experience drastic changes throughout their lifetimes, and evolution should be considered.

Acknowledgments

Y.M. acknowledges support from the European Research Council (ERC) under the European Union's Horizon 2020 research and innovation program (grant agreement No. 101088557, N-GINE).

We would also like to thank Sam de Regt and Siddharth Ghandi for their useful discussions.

ORCID iDs

Amy J. Louca https://orcid.org/0000-0002-3191-2200
Yamila Miguel https://orcid.org/0000-0002-0747-8862

References

Alderson, L., Wakeford, H. R., Alam, M. K., et al. 2023, Natur, 614, 664
Alei, E., Konrad, B. S., Angerhausen, D., et al. 2022, A&A, 665, A106
Allard, N. F., Spiegelman, F., & Kielkopf, J. F. 2016, A&A, 589, A21
Allard, N. F., Spiegelman, F., Leininger, T., & Molliere, P. 2019, A&A, 628, A120
Asplund, M., Grevesse, N., Sauval, A. J., & Scott, P. 2009, ARA&A, 47, 481
Azzam, A. A. A., Tennyson, J., Yurchenko, S. N., & Naumenko, O. V. 2016, MNRAS, 460, 4063
Batalha, N. E., Mandell, A., Pontoppidan, K., et al. 2017, PASP, 129, 064501
Bean, J. L., Xue, Q., August, P. C., et al. 2023, Natur, 618, 43
Bergin, E. A., Kempton, E. M. R., Hirschmann, M., et al. 2023, ApJL, 949, L17
Catling, D., & Kasting, J. 2017, Atmospheric Evolution on Inhabited and Lifeless Worlds (Cambridge: Cambridge Univ. Press)
Choi, J., Dotter, A., Conroy, C., et al. 2016, ApJ, 823, 102
Chubb, K. L., Naumenko, O., Keely, S., et al. 2018, JQSRT, 218, 178
Coles, P. A., Yurchenko, S. N., & Tennyson, J. 2019, MNRAS, 490, 4638
Dos Santos, L. A. 2023, in IAU Symp. 370, Winds of Stars and Exoplanets, ed. A. A. Vidotto, L. Fossati, & J. S. Vink (Cambridge: Cambridge Univ. Press), 56
Dotter, A. 2016, ApJS, 222, 8
Gueymard, C. A. 2003, SoEn, 74, 355
Gupta, A., & Schlichting, H. E. 2019, MNRAS, 487, 24
Hunten, D. M., Pepin, R. O., & Walker, J. C. G. 1987, Icar, 69, 532
Jermyn, A. S., Bauer, E. B., Schwab, J., et al. 2023, ApJS, 265, 15
Johnstone, C. P., Güdel, M., Stökl, A., et al. 2015, ApJL, 815, L12
Kubyshkina, D., Fossati, L., Erkaev, N. V., et al. 2018, ApJL, 866, L18
Kubyshkina, D., Vidotto, A. A., Fossati, L., & Farrell, E. 2020, MNRAS, 499, 77
Kurucz, R. L., & Bell, B. 1995, Atomic Line List (Cambridge, MA: Smithsonian Astrophysical Observatory)
Li, G., Gordon, I. E., Rothman, L. S., et al. 2015, ApJS, 216, 15
Linsky, J. L., Yang, H., France, K., et al. 2010, ApJ, 717, 1291
Lodders, K., & Fegley, B. 2002, Icar, 155, 393
Louca, A. J., Miguel, Y., Tsai, S.-M., et al. 2023, MNRAS, 521, 3333
Malik, M., Grosheintz, L., Mendonça, J. M., et al. 2017, AJ, 153, 56
Malik, M., Kitzmann, D., Mendonça, J. M., et al. 2019, AJ, 157, 170
Malsky, I., & Rogers, L. 2020, ApJ, 896, 48
Mankovich, C. R., & Fuller, J. 2021, NatAs, 5, 1103
Marrero, T. R., & Mason, E. A. 2009, JPCRD, 1, 3
Miguel, Y., Bazot, M., Guillot, T., et al. 2022, A&A, 662, A18
Miguel, Y., & Kaltenegger, L. 2014, ApJ, 780, 166
Modirrousta-Galian, D., & Korenaga, J. 2023, ApJ, 943, 11
Mollière, P., Stolker, T., Lacour, S., et al. 2020, A&A, 640, A131
Mollière, P., Wardenier, J. P., van Boekel, R., et al. 2019, A&A, 627, A67
Mordasini, C., van Boekel, R., Mollière, P., Henning, T., & Benneke, B. 2016, ApJ, 832, 41
Moses, J. I., Line, M. R., Visscher, C., et al. 2013, ApJ, 777, 34
Öberg, K. I., Murray-Clay, R., & Bergin, E. A. 2011, ApJL, 743, L16
Pacetti, E., Turrini, D., Schisano, E., et al. 2022, ApJ, 937, 36
Parmentier, V., Showman, A., & Lian, Y. 2013, A&A, 558, A91
Paxton, B., Bildsten, L., Dotter, A., et al. 2011, ApJS, 192, 3
Paxton, B., Cantiello, M., Arras, P., et al. 2013, ApJS, 208, 4
Paxton, B., Marchant, P., Schwab, J., et al. 2015, ApJS, 220, 15
Paxton, B., Schwab, J., Bauer, E. B., et al. 2018, ApJS, 234, 34

Paxton, B., Smolec, R., Schwab, J., et al. 2019, ApJS, 243, 10
Piskunov, N. E., Kupka, F., Ryabchikova, T. A., Weiss, W. W., & Jeffery, C. S. 1995, A&AS, 112, 525
Polman, J., Waters, L. B. F. M., Min, M., Miguel, Y., & Khorshid, N. 2023, A&A, 670, A161
Polyansky, O. L., Kyuberis, A. A., Zobov, N. F., et al. 2018, MNRAS, 480, 2597
Rothman, L., Gordon, I., Barber, R., et al. 2010, JQSRT, 111, 2139
Roueff, E., Abgrall, H., Czachorowski, P., et al. 2019, A&A, 630, A58
Schlawin, E., Agol, E., Walkowicz, L. M., Covey, K., & Lloyd, J. P. 2010, ApJL, 722, L75
Somogyi, W., Yurchenko, S. N., & Yachmenev, A. 2021, JChPh, 155, 214303
Sousa-Silva, C., Al-Refaie, A. F., Tennyson, J., & Yurchenko, S. N. 2014, MNRAS, 446, 2337
Stock, J., Kitzmann, D., Patzer, A., & Sedlmayr, E. 2018, MNRAS, 479, 865
Tashkun, S., & Perevalov, V. 2011, JQSRT, 112, 1403
Tsai, S.-M., Lee, E. K. H., Powell, D., et al. 2023, Natur, 1476
Tsai, S.-M., Lyons, J. R., Grosheintz, L., et al. 2017, ApJS, 228, 20
Tsai, S.-M., Malik, M., Kitzmann, D., et al. 2021, ApJ, 923, 264
Turrini, D., Schisano, E., Fonte, S., et al. 2021, ApJ, 909, 40
Underwood, D. S., Tennyson, J., Yurchenko, S. N., et al. 2016, MNRAS, 459, 3890
Vidal-Madjar, A., Désert, J. M., Lecavelier des Etangs, A., et al. 2004, ApJL, 604, L69
Wahl, S. M., Hubbard, W. B., Militzer, B., et al. 2017, GeoRL, 44, 4649
Yurchenko, S. N., Amundsen, D. S., Tennyson, J., & Waldmann, I. P. 2017, A&A, 605, A95
Yurchenko, S. N., Mellor, T. M., Freedman, R. S., & Tennyson, J. 2020, MNRAS, 496, 5282
Yurchenko, S. N., & Tennyson, J. 2014, MNRAS, 440, 1649
Zahnle, K., Marley, M. S., Freedman, R. S., Lodders, K., & Fortney, J. J. 2009, ApJL, 701, L20